https://doi.org/10.5194/egusphere-2026-5511
Preprint. Discussion started: 16 September 2026

First simultaneous retrieval of O_2 A-band nightglow volume emission rate and temperature in the MLT from Tianlu-1/HDI hyperspectral observations

Guoyin Zeng[1,2,3], Haiyan Luo[2,3], Wei Xiong[1,2,3], Zhiwei Li[2,3], Qiansheng Wang[2,3], Yida Qian[1,2,3], Qiong Wu[1,2,3], Yi Ding[2,3], Wenhui Luo[2,3]

[1]School of Environmental Science and Optoelectronic Technology, University of Science and Technology of China, Hefei 230026, China
[2]Anhui Institute of Optics and Fine Mechanics, Hefei Institutes of Physical Science, Chinese Academy of Sciences, Hefei 230031, China
[3]Anhui Province Key Laboratory of Optical Quantitative Remote Sensing, Hefei Institutes of Physical Science, Chinese Academy of Sciences, Hefei 230031, China

Correspondence to: Haiyan Luo (luohaiyan@aiofm.ac.cn)

Abstract. The O_2 A-band nightglow contains complementary information on volume emission rate (VER) and temperature in the mesosphere and lower thermosphere (MLT), yet their simultaneous retrieval remains challenging because it requires detecting weak airglow emissions while resolving temperature-sensitive rotational structures. The Hyperspectral Atmospheric Density Imager (HDI), launched aboard Tianlu-1 in January 2025, is China's first spaceborne limb-sounding payload based on spatial heterodyne spectroscopy and provides hyperspectral limb observations of the O_2 A-band nightglow at a spectral resolution as fine as 0.0394 nm, enabling detailed characterization of its rotational structure. Here, we present a joint algorithm for simultaneous nighttime VER and temperature retrieval and demonstrate its performance using early on-orbit HDI measurements. Results show stable simultaneous retrievals during selected nighttime windows over 86–98 km. Retrieved VER distributions are consistent with the expected primary O_2 A-band emission layer. HDI temperatures agree with collocated, window-averaged SABER observations, with monthly mean absolute differences below 3.82 K. Monthly mean posterior 1σ uncertainties are below 5.09% for VER and 3.51 K for temperature, with monthly mean temperature degrees of freedom for signal exceeding 0.946. These results demonstrate, for the first time, the simultaneous retrieval of nighttime VER and temperature from individual hyperspectral measurements, providing intrinsically co-registered and internally consistent constraints for subsequent photochemical retrievals of atomic oxygen. This advance establishes a new spaceborne capability for characterizing the coupled thermal–photochemical state of the MLT and investigating interactions among atmospheric chemistry, radiation, and dynamics in this region.

https://doi.org/10.5194/egusphere-2026-5511
Preprint. Discussion started: 16 September 2026

1 Introduction

The Hyperspectral Atmospheric Density Imager (HDI) is China's first spaceborne limb-sounding payload based on spatial heterodyne spectroscopy (SHS). It is one of the payloads onboard the Tianlu-1 satellite, which was launched into orbit on 17 January 2025 at a nominal orbital altitude of approximately 520 km (Luo et al., 2025). HDI provides an instantaneous vertical atmospheric imaging coverage of approximately 102.86 km, with a spectral range of 756.8–771.4 nm and a measured spectral resolution of up to 0.0394 nm, enabling hyperspectral measurements of the O_2 A band. The original HDI mission was primarily designed for daytime atmospheric density profiling in the 20–70 km altitude range, by observing O_2 A-band absorption features in solar backscattered atmospheric radiation. Benefiting from the stable thermal-control performance of the payload, particularly the stability of detector cooling, HDI has successfully acquired fine spectral measurements of O_2 A-band nightglow in the mesosphere and lower thermosphere (MLT) under nighttime limb-viewing conditions after increasing the on-orbit integration time.

The MLT is commonly regarded as an atmospheric transition region at approximately 80–110 km above the Earth's surface (Katsuda et al., 2023), characterized by pronounced atmospheric wave activity, tidal motions, and photochemical reactions (Van Caspel et al., 2023; Plane et al., 2015; He and Forbes, 2022; Jia et al., 2024). Accurate measurements of key atmospheric parameters in this region are fundamental for understanding the thermal structure, dynamical transport, photochemical processes, and their couplings in the middle and upper atmosphere (Wu et al., 2026). The O_2 A-band nightglow is an important optical tracer in the nighttime MLT and is mainly produced by the $O_2(b^1\Sigma_g^+, v=0) \rightarrow O_2(X^3\Sigma_g^-)$ transition excited (Kvifte, 1951) through the Barth mechanism (Kalogerakis, 2019). Its volume emission rate (VER) is closely related to atomic oxygen abundance and associated transport processes (Zarboo et al., 2018), while the relative intensities of the rotational lines in the O_2 A-band airglow are sensitive to temperature variations (Wu et al., 2024). Therefore, high-precision measurements of fine spectral features in O_2 A-band nightglow can provide an important observational basis for investigating the atomic oxygen distribution and vertical temperature structure in the nighttime MLT.

However, compared with dayglow, nighttime O_2 A-band emissions are relatively weak, making both the airglow radiance information and the temperature-sensitive rotational-line structure more difficult to retrieve robustly (Linder et al., 2025). Therefore, the simultaneous extraction of reliable VER information and temperature-sensitive rotational spectral information from the same spaceborne O_2 A-band observation remains a key challenge for achieving high-precision joint retrievals of O_2 A-band nightglow VER and nighttime MLT temperature. The Optical Spectrograph and Infrared Imaging System (OSIRIS) onboard the Swedish Odin satellite and the SCanning Imaging Absorption spectroMeter for Atmospheric CHartographY (SCIAMACHY) onboard the Environmental Satellite (Envisat) have both performed limb-spectral observations of O_2 A-band airglow, with spectral resolutions near the O_2 A band of approximately 1 nm (Sheese, 2011) and 0.48 nm (Hamidouche and Lichtenberg, 2018), respectively. Based on OSIRIS O_2 A-band airglow spectra, Sheese et al. (2010) retrieved temperatures in the MLT region. Under dayglow conditions, the systematic temperature retrieval errors at and above 90 km were approximately ±2–±6 K, with posterior retrieval errors of about ±4–±15 K; however, the temperature retrieval uncertainty increased

https://doi.org/10.5194/egusphere-2026-5511
Preprint. Discussion started: 16 September 2026

substantially under weak nightglow conditions. Atomic oxygen concentrations retrieved from SCIAMACHY O_2 A-band nightglow integrated radiances were found to agree within approximately 15% with those derived from other SCIAMACHY nightglow proxy measurements (Richter et al., 2021; Zhu and Kaufmann, 2019). Nevertheless, the spectral resolutions of OSIRIS and SCIAMACHY are insufficient to fully resolve individual rotational lines and fine spectral structures in the O_2 A-band, particularly under weak nighttime emission conditions (Zhu and Kaufmann, 2019).

In recent years, multi-channel filter-imaging instruments have further expanded spaceborne observational capabilities for O_2 A-band airglow. The Michelson Interferometer for Global High-resolution Thermospheric Imaging (MIGHTI) onboard the Ionospheric Connection Explorer (ICON) satellite measures O_2 A-band signal intensities in different spectral passbands using multiple filter channels with prescribed spectral response functions, and retrieves MLT temperatures from the relative intensity variations among these channels. Its nighttime retrieved temperatures over 90–105 km shows mean differences of less than 7 K compared with temperature products from the Sounding of the Atmosphere using Broadband Emission Radiometry (SABER) (Stevens et al., 2022; Remsberg et al., 2008). The Mesospheric Airglow/Aerosol Tomography and Spectroscopy (MATS) satellite also observes O_2 A-band airglow using multi-channel filter-based limb imaging, and retrieves O_2 A-band airglow VER profiles from calibrated images (Gumbel et al., 2020; Linder et al., 2025). While these filter-based instruments have greatly advanced spaceborne O_2 A-band airglow imaging, continuous high-resolution spectroscopic observations can further retain the detailed rotational spectral structures of the band, thereby providing additional information for temperature-sensitive spectral analysis and joint VER–temperature retrievals.

Spaceborne O_2 A-band limb-sounding instruments based on SHS, including AtmoSHINE and AtmoLITE, have undergone in-orbit technology demonstrations or related mission implementations, demonstrating the potential of exploiting the fine spectral structure of the O_2 A-band for MLT temperature sounding (Liu, 2019; Ntokas et al., 2023). However, publicly available studies have primarily focused on instrument validation, forward simulations, or assessments of temperature retrieval capability (Liu, 2019; Ntokas et al., 2023; Chen et al., 2022). Applications involving the simultaneous retrieval of VER and temperature from spaceborne high-resolution O_2 A-band nightglow measurements under weak nighttime emission conditions remain limited. In this context, HDI, as one of the earliest spaceborne payloads to demonstrate in-orbit observations of high-resolution O_2 A-band nightglow spectra, provides a new observational basis for the simultaneous retrieval of nightglow VER and MLT temperature under weak nightglow conditions.

Consequently, previous photochemical retrievals of atomic oxygen from O_2 A-band nightglow VER have typically relied on externally supplied temperature and background-density profiles, potentially introducing inconsistencies associated with differences in sampling time, location, vertical resolution, and viewing geometry (Zhu and Kaufmann, 2019). Using hyperspectral O_2 A-band nightglow observations acquired by HDI, this study develops a physically consistent joint retrieval framework for VER and temperature based on the fine rotational spectral structure of the O_2 A-band. The retrieval algorithm is applied to the first effective nighttime observations acquired by HDI during May–August 2025 to derive O_2 A-band nightglow VER and MLT temperature. The retrieved temperatures are independently evaluated against temperature products from the SABER. In addition, posterior uncertainties and the degrees of freedom for signal (DOFS) are analysed to quantify

https://doi.org/10.5194/egusphere-2026-5511
Preprint. Discussion started: 16 September 2026

the capability of fine O_2 A-band spectral structures to simultaneously constrain VER and temperature under weak nightglow conditions.

2 Methods

2.1 HDI nighttime limb observations, retrieval, and valid-frame selection

Figure 1 illustrates the observation and retrieval workflow of HDI based on SHS. The HDI limb-viewing observation model is established under the assumption of a spherically symmetric, layered atmosphere (Deiml, 2017). The two-dimensional focal-plane array (FPA) simultaneously records atmospheric information along the vertical dimension and hyperspectral interferometric information along the spectral dimension, allowing each observation frame to provide limb spectra over the entire observed altitude range with temporal sampling interval of approximately 11 seconds. HDI has a vertical field of view of 2.368°, corresponding to an atmospheric vertical coverage of approximately 102.86 km with an original vertical sampling interval of about 0.1 km.

Because the orbital altitude, platform attitude, and viewing geometry vary throughout the mission, the atmospheric altitude range covered by individual observation frames is not identical, although the upper boundary of the field of view is consistently above approximately 98 km. Consequently, the quantitative retrieval analysis presented here is restricted to the 86–98 km altitude range, where the O_2 A-band nightglow emission is sufficiently strong (Hays et al., 2003), the vertical coverage is consistent among observations, and the spectral information content is adequate for stable simultaneous retrieval of VER and temperature.

A triangular apodization window was then applied to the interferometric signal at each altitude level to suppress spectral sidelobes caused by finite optical path difference truncation (Shi et al., 2020) and to improve the stability of spectral reconstruction and retrieval under weak nightglow conditions. The effective spectral resolution of the reconstructed spectra after apodization is approximately 0.057 nm. Given the weak nighttime O_2 A-band airglow signal, the spectra reconstructed from 20 adjacent detector rows along the atmospheric vertical direction were averaged, resulting in an altitude spacing of approximately 2 km.

The primary on-orbit mission of HDI is atmospheric density profile sounding in the 20–70 km altitude range. Nighttime O_2 A-band airglow observations were obtained as the first effective dataset under specific observation parameters and operating modes. The HDI nightglow observations used in this study were acquired during four observation windows from May to August 2025: 8–14 May, 19–25 June, 12–18 July, and 1–7 August 2025. Each observation window lasted approximately one week. To select nighttime observations suitable for O_2 A-band nightglow retrieval within each observation window, a solar zenith angle (SZA) greater than 100° was used as the nighttime criterion (Sun et al., 2022), and HDI frames satisfying this condition were selected as valid observation frames for nighttime retrieval.

After background subtraction, the apodized and reconstructed HDI spectra over 86–98 km, were used for joint retrieval analysis together with the O_2 A-band nightglow forward model developed in this study. The retrieval procedure first applies

https://doi.org/10.5194/egusphere-2026-5511
Preprint. Discussion started: 16 September 2026

an unconstrained linear inversion without a priori information and without accounting for self-absorption (Liou, 2002), to rapidly estimate the O_2 A-band nightglow VER profile within the target altitude range. This estimate is then used as the initial a priori profile for the subsequent nonlinear optimal estimation retrieval. The VER and temperature profiles are then retrieved simultaneously using an optimal estimation algorithm based on Levenberg–Marquardt (L–M) iteration (Rodgers, 2000). The retrieval state vector includes the VER profile, temperature profile, O_2 number density profile, wavelength shift, and spectral resolution. Among these parameters, VER and temperature are the primary retrieval targets. The temperature and O_2 number density profiles are constrained by a priori profiles from the Mass Spectrometer and Incoherent Scatter (MSIS) model (Picone et al., 2002). The O_2 number density profile is mainly used to represent self-absorption effects in the O_2 A-band nightglow. The wavelength shift and spectral resolution are treated as auxiliary parameters related to spectral calibration and the instrumental line shape, and are included to improve the agreement between the measured and forward-modelled spectra.

https://doi.org/10.5194/egusphere-2026-5511
Preprint. Discussion started: 16 September 2026

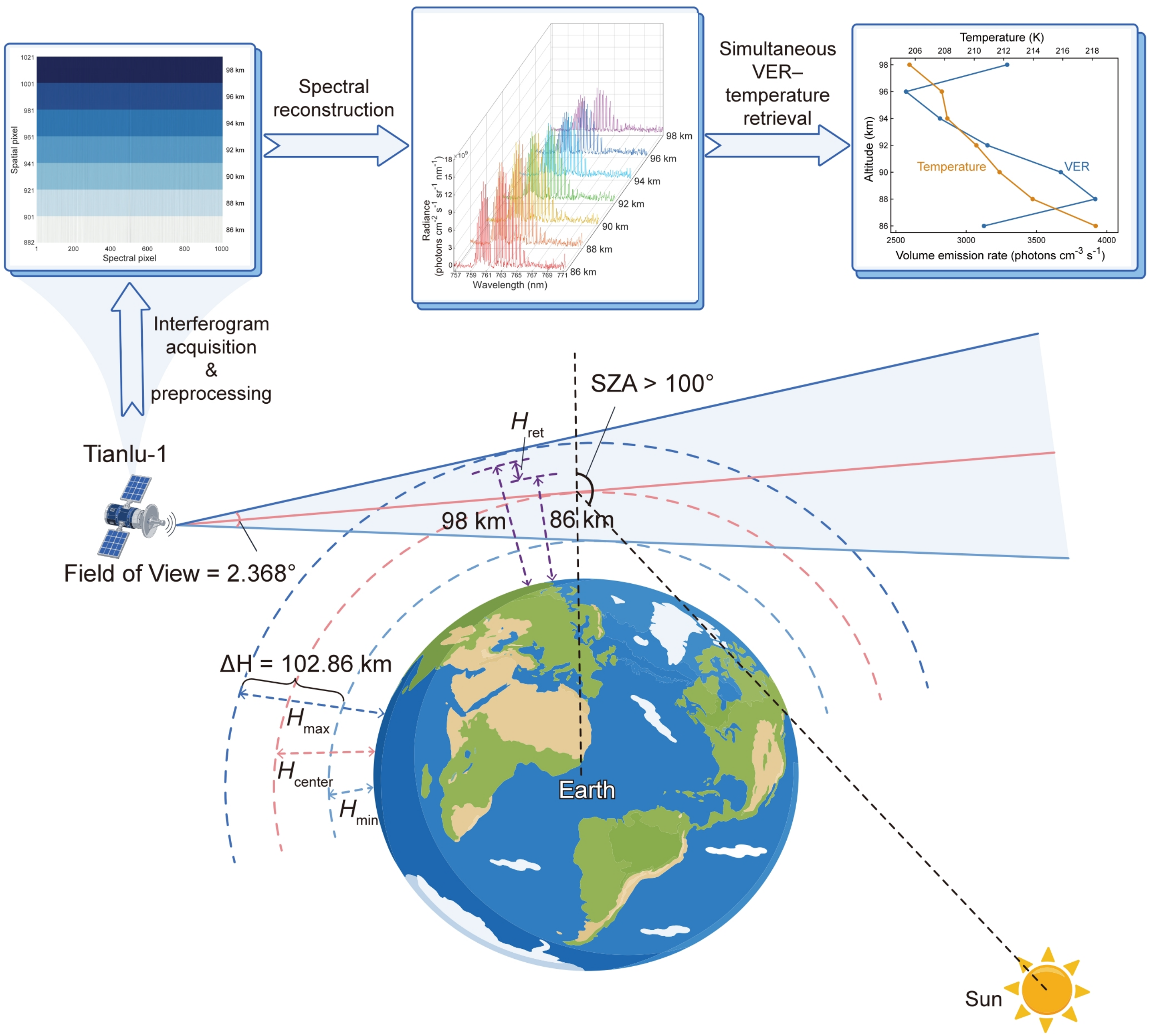

Figure 1. Schematic overview of HDI on-orbit limb viewing, interferogram acquisition, spectral preprocessing and reconstruction, and simultaneous VER–temperature retrieval. The altitude coverage of each frame is determined by the vertical field of view. Based on the tangent height at the center of the payload boresight, H_{center}, the minimum and maximum tangent heights, H_{min} and H_{max}, are calculated for different lines of sight within the single-frame limb-viewing field. The resulting vertical tangent-height coverage is approximately 102.86 km. H_{ret} denotes the retrieval altitude range from 86 to 98 km. The example interferograms and reconstructed spectra were acquired at 08:25:09 UTC on 8 May 2025 at 82.47°S, 53.35°W. The schematic is not to scale.

Figure 2 presents an example of the HDI observation tracks on 12 May 2025 UTC. The gray dashed lines indicate observation frames with valid geolocation information on that day, while the black solid lines denote the valid observation frames satisfying

https://doi.org/10.5194/egusphere-2026-5511
Preprint. Discussion started: 16 September 2026

the SZA > 100° criterion and selected for O_2 A-band nightglow retrieval. The gaps in the tracks correspond to periods when the platform was in a non-imaging operating state after the satellite entered the Earth's shadow, during which HDI did not acquire valid observation frames.

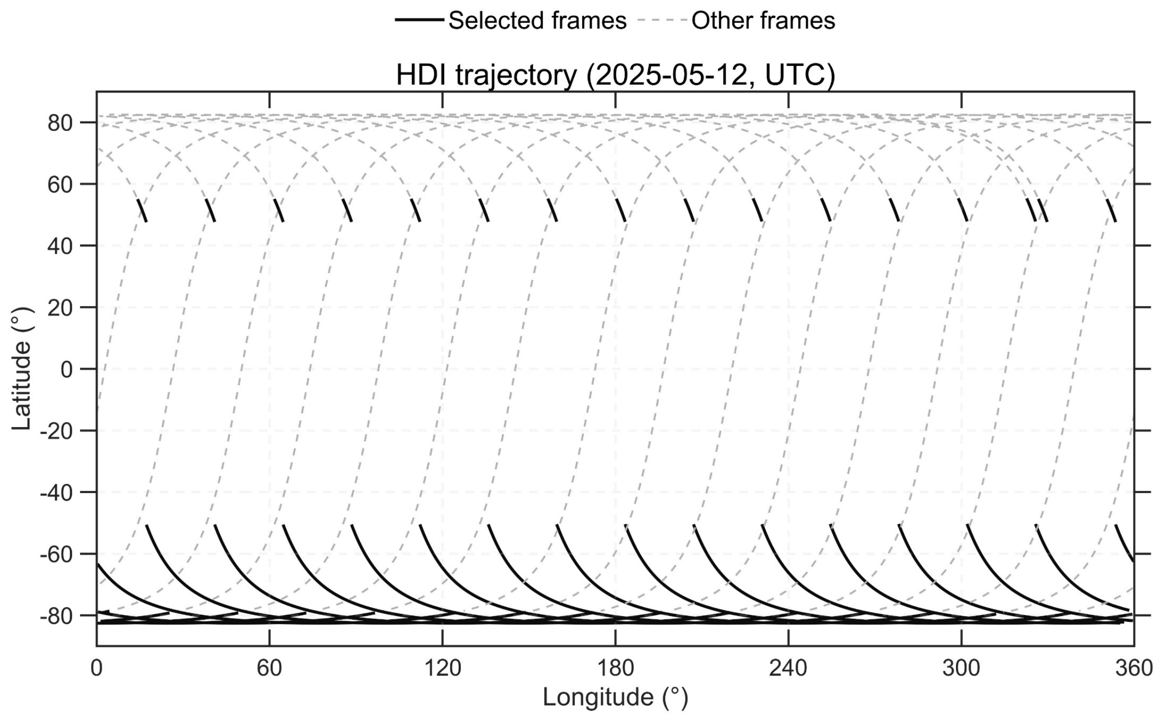

Figure 2. HDI observation tracks on 12 May 2025 UTC. The track locations indicate the geographic positions of the reference tangent point for each frame.

2.2 Apodized HDI instrumental line shape and spectral background removal

The instrumental line-shape (ILS) function reconstructed from the raw HDI interferograms under a finite maximum optical path difference can be approximated by a sinc function. Without apodization, the spectral resolution of HDI can reach 0.0394 nm, but the sidelobe structure of the sinc-like ILS may affect the fitting of weak nightglow emission lines (Shi et al., 2020). To suppress sidelobe effects caused by finite optical path difference truncation while preserving the spectral resolution as much as possible, a triangular apodization window was applied to the interferograms prior to spectral reconstruction. After triangular apodization, the effective ILS of HDI can be approximated by a $sinc^2$ function, with an effective in-orbit FWHM of approximately 0.057 nm.

The spectral background mainly consists of continuum scattered light, dark background, and low-frequency radiance baseline components. To reduce the influence of background contributions on the fitting of weak O_2 A-band nightglow lines, the wavelength intervals of 756.8–759.0 nm and 767.0–771.4 nm were used as background constraint regions. A linear background

https://doi.org/10.5194/egusphere-2026-5511
Preprint. Discussion started: 16 September 2026

was fitted and subtracted for each limb spectrum (Sun et al., 2022). The subsequent VER and temperature retrievals were performed using the background-subtracted O_2 A-band spectra, with the retrieval window set to 759.58–767.00 nm.

2.3 Forward model

The O_2 A-band nightglow emission spectrum contains dense rotational emission structures, and the relative intensities of different rotational lines vary with temperature (Noll et al., 2016). Under thermal equilibrium, the rotational transition spectrum of the O_2 A-band nightglow follows a Boltzmann distribution at the rotational temperature T (Russell and Lowe, 2003). Therefore, the photon number $\varepsilon(v_0)$ of a rotational line at a given wavenumber v_0 can be calculated as follows:

$$\varepsilon(v_0) = \frac{A_{v_0}(2J_{v_0}'+1)\exp(-hcE_{v_0}'/kT)}{Q_{\text{tot}}^{\text{up}}(T)}, \tag{1}$$

where the Einstein coefficient A_{v_0}, upper-state energy E_{v_0}', and total angular momentum quantum number of the upper state J_{v_0}' are taken from the High Resolution Transmission (HITRAN) database (Kochanov et al., 2016). h, c, and k denote the Planck constant, the speed of light in vacuum, and the Boltzmann constant, respectively. $Q_{\text{tot}}^{\text{up}}(T)$ is the partition sum of $O_2(\text{b}^1\Sigma_g^+, \text{v}=0)$ (Yu et al., 2014).

Because the atmospheric pressure in the MLT is low, collisional broadening is substantially reduced. Pressure broadening is therefore negligible compared with Doppler broadening. Based on the calculated O_2 A-band airglow emission-line intensities, the spectral VER of O_2 A-band nightglow at altitude H, can be expressed as:

$$\eta(v_0, H) = \varepsilon(v_0, H) \times \text{VER}_{O_2(\text{b}^1\Sigma_g^+)}(H) D(v, T), \tag{2}$$

where $\varepsilon(v_0, H)$ and $\text{VER}_{O_2(\text{b}^1\Sigma_g^+)}$ denote the O_2 A-band nightglow spectral emission rate and the vertically resolved VER at H, respectively, and $D(v,T)$ is the Doppler-broadened line-shape function.

In this model, the Earth is approximated as an ideal sphere, the atmosphere is divided into concentric spherical shells, and the atmospheric temperature, molecular number densities, and atomic number densities are assumed to be constant within each layer. In the OSIRIS-based O_2 A-band airglow temperature retrieval (Sheese et al., 2010) and the MIGHTI temperature forward–retrieval framework (Stevens et al., 2022), O_2 A-band airglow self-absorption was neglected or treated as a weak effect because the analysed altitudes were mainly above approximately 90 km, and the spectral information was limited by relatively coarse spectral resolution or by the use of filter-channel integrated intensities. Under this approximation, the entrance-aperture spectral radiance observed by HDI at tangent height H_i can be expressed as the line-of-sight (LOS) integral of the VER contributions from each atmospheric layer (Li et al., 2023):

$$R(v_0, H_i) = \frac{1}{4\pi}\int_{\text{LOS}(H_i)} \eta(v_0, s)\,\text{d}s, \tag{3}$$

https://doi.org/10.5194/egusphere-2026-5511
Preprint. Discussion started: 16 September 2026

However, for the continuous high-resolution O_2 A-band nightglow spectra acquired by HDI, although O_2 A-band self-absorption is generally weak in the MLT, its effect is not identical for different rotational lines. It may still modify the relative intensities among spectral lines and thereby affect the accuracy of the simulated temperature-sensitive spectral structures. Therefore, self-absorption along the LOS propagation path is included in the O_2 A-band nightglow limb radiative-transfer model used in this study. The entrance-aperture spectral radiance of O_2 A-band nightglow observed at H_i, can be calculated as:

$$R(v_0, H_i) = \frac{1}{4\pi}\int_{\mathrm{LOS}(H_i)} \eta(v_0, s)\exp[-\int_s^{obs} \alpha_{\mathrm{O_2}}(v_0, s')\mathrm{d}s']\mathrm{d}s\,, \tag{4}$$

where the exponential term represents the transmission from the emission location s to the HDI entrance aperture and accounts for self-absorption along the LOS (Sun et al., 2022).

Accordingly, in the wavelength domain, the spectral radiance measured by HDI, can be expressed as the convolution of the entrance-aperture spectral radiance with the HDI instrumental line-shape function:

$$R_{\mathrm{HDI}}(\lambda, H_i) = R(\lambda, H_i) \otimes \mathrm{ILS}_{\mathrm{HDI}}\,, \tag{5}$$

2.4 Retrieval algorithm

In the linear initialization step, self-absorption of O_2 A-band nightglow photons along the limb LOS is neglected. The matrix form of Eq. (3) is then solved directly using unconstrained least squares to obtain the local VER spectrum for each atmospheric layer:

$$\eta = 4\pi(\mathrm{L}^{\mathrm{T}}\mathrm{L})^{-1}\mathrm{L}^{\mathrm{T}} R_{\mathrm{HDI}}\,, \tag{6}$$

where, L is the path-length matrix describing the intersections of the limb LOS with the individual atmospheric layers (Sun et al., 2018).

The layer-resolved local VER spectra are then integrated over wavelength to obtain the initial O_2 A-band nightglow VER profile at each altitude level. This profile is used as the a priori constraint for the subsequent L–M optimal estimation retrieval. The objective of the optimal estimation retrieval is to obtain a statistically optimal balance between the measurement constraints and the a priori constraints by minimizing the following cost function (Rodgers, 2000; Xing et al., 2025):

$$J(x) = [y - \mathrm{F}(x)]^{\mathrm{T}} S_e^{-1}[y - \mathrm{F}(x)] + [x - x_a]^{\mathrm{T}} S_a^{-1}[x - x_a]\,, \tag{7}$$

where x_a is the a priori state vector, S_a is the a priori error covariance matrix, and S_e is the measurement error covariance matrix.

The L–M method is used to iteratively minimize the cost function. The state-vector update at the i+1-th iteration can be written as:

$$x_{i+1} = x_i + [(1+\gamma)S_a^{-1} + K_i^{\mathrm{T}} S_e^{-1} K_i]^{-1}\{K_i^{\mathrm{T}} S_e^{-1}[y - \mathrm{F}(x_i)] - S_a^{-1}[x_i - x_a]\}\,, \tag{8}$$

where $K_i = \partial \mathrm{F}/\partial x$ is the Jacobian matrix at the i-th iteration, representing the sensitivity of the simulated spectra to the retrieval parameters, and γ is the L–M damping parameter.

https://doi.org/10.5194/egusphere-2026-5511
Preprint. Discussion started: 16 September 2026

After convergence, the posterior error covariance matrix can be written as:

$$\hat{S} = (K^{\mathrm{T}} S_e^{-1} K + S_a^{-1})^{-1} , \tag{9}$$

where K is the Jacobian matrix evaluated at the final retrieved state. The posterior uncertainty of each retrieved parameter is given by the square root of the corresponding diagonal element of $\hat{S}$.

To evaluate the independent constraint provided by the measured spectra on the retrieval results, the averaging kernel matrix is further calculated as:

$$A = \hat{S} K^{\mathrm{T}} S_e^{-1} K , \tag{10}$$

The diagonal elements of A quantify the information content, or DOFS contribution, for each state-vector element. Values close to 1 indicate that the corresponding parameter is primarily constrained by the measured spectra, whereas lower values indicate greater sensitivity to the a priori constraint.

3 Result

3.1 Local joint retrieval from fine HDI O_2 A-band nightglow spectra

Figure 3 presents a representative retrieval result for a local observation in the Southern Hemisphere (SH). The HDI observation frame was acquired at 20:12:05 UTC on 12 May 2025, at 50.51°S and 40.94°E. Figure 3a shows the measured HDI spectra, fitted spectra, and residuals at four representative altitude levels of 86, 90, 94, and 98 km. The fitted spectra reproduce the main rotational-line structures of the observed O_2 A-band nightglow well, including the positions, line shapes, and relative intensities of the strong emission lines at different altitudes. The corresponding residuals fluctuate around zero and show no evident systematic line-shaped structures. For all four altitude levels, the normalized root mean square errors (RMSEs) of the spectral fits, relative to the peak values of the measured spectra, are below 2%. These results indicate that the forward model developed in this study can robustly represent the fine spectral structure of HDI O_2 A-band nightglow at different altitude levels.

Figure 3b shows the retrieved O_2 A-band nightglow VER and temperature profiles for this observation frame, together with their posterior 1σ uncertainties. The a priori VER profile was rapidly estimated using the linear inversion, and its overall profile shape is generally consistent with the result obtained from the L–M optimal estimation retrieval. Because the linear inversion does not explicitly account for O_2 A-band nightglow self-absorption, the a priori VER values below 90 km are generally lower than the final iterative retrieval results. The final retrieved VER shows a pronounced enhancement over 88–92 km, with a peak near 90 km, and then gradually decreases with increasing altitude. Within 86–98 km, the retrieved VER ranges from 1110.10 to 2775.67 photons cm^{-3} s^{-1}. The relative posterior 1σ uncertainty ranges from 0.95% to 4.29%, with larger relative errors at lower altitudes and an overall decrease with altitude.

Figure 3b also shows the SABER temperature profile spatiotemporally collocated with the HDI observation, which is used as an independent temperature reference. The corresponding SABER event is 127116, observed at 20:15:16 UTC on 12 May

https://doi.org/10.5194/egusphere-2026-5511
Preprint. Discussion started: 16 September 2026

2025 at 50.34°S and 40.81°E. Over 86–98 km, the HDI-retrieved temperature generally decreases from 86 to 94 km, reaches a minimum near 94 km, and then increases again at 96–98 km. This vertical structure is broadly consistent with the SABER temperature profile. Within this altitude range, the HDI-retrieved temperature is 169.33 to 211.04 K, while the SABER temperature is 164.82 to 211.24 K. The temperature differences range from −7.26 to 4.51 K, with a mean absolute difference of 4.47 K. The posterior 1σ uncertainty of the HDI temperature ranges from 1.63 to 3.02 K, with the largest uncertainty at 86 km. Compared with the MSIS a priori profile, the HDI-retrieved temperature is generally closer to the independent SABER observation, indicating that the measured O_2 A-band rotational spectral structure provides effective observational constraints on the temperature retrieval, rather than the result being primarily prior-dominated.

The DOFS for VER at each altitude level from 86 to 98 km is close to 1.000, indicating that VER in this case is effectively constrained by the measured HDI spectra. The temperature DOFS also remains high, ranging from 0.956 to 1.000. This is consistent with the clear update of the retrieved temperature relative to the MSIS a priori profile and its improved agreement with the independent SABER observation.

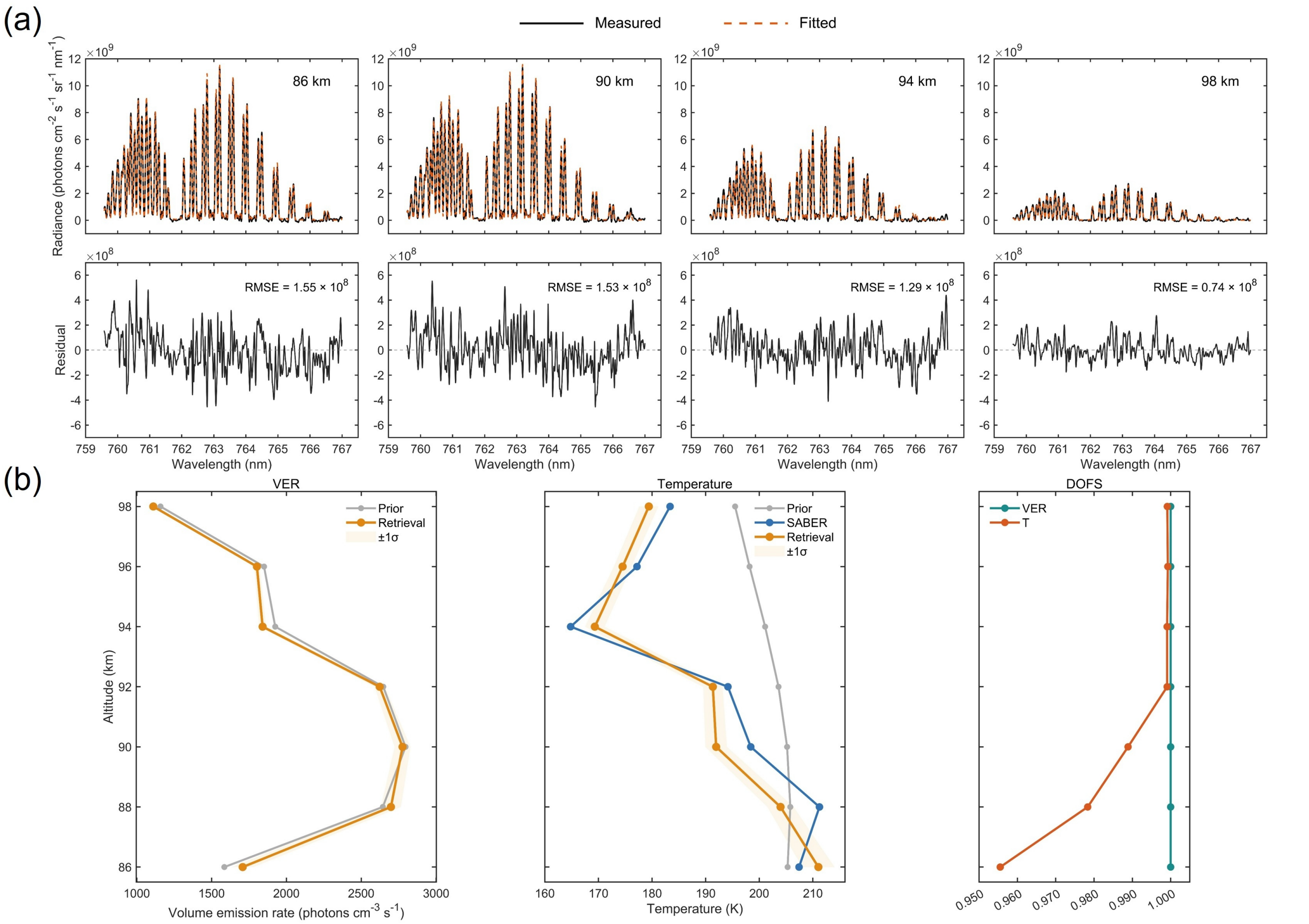

https://doi.org/10.5194/egusphere-2026-5511
Preprint. Discussion started: 16 September 2026

Figure 3. Simultaneous retrieval of O_2 A-band nightglow from a representative SH HDI observation. (a) Measured HDI spectra, fitted spectra, and residuals at 86, 90, 94, and 98 km. (**b)** Retrieved O_2 A-band nightglow VER and temperature profiles, together with the corresponding DOFS. The HDI observation was acquired at 20:12:05 UTC on 12 May 2025 at 50.51°S, 40.94°E. The collocated SABER event is 127116, observed at 20:15:16 UTC on 12 May 2025 at 50.34°S, 40.81°E.

Figure 4 presents the retrieval results for a local observation in the Northern Hemisphere (NH). The HDI observation frame was acquired at 05:21:58 UTC on 10 May 2025, at 55.07°N and 116.38°W. In Figure 4a, the fitted spectra also reproduce the main rotational-line structures of the measured O_2 A-band nightglow well, and the residuals show no evident systematic line-shaped structures.

Figure 4b shows that the retrieved VER increases markedly with altitude from 86 to 94 km, reaches a peak near 94 km, and then gradually decreases over 96–98 km, exhibiting a typical vertical distribution of O_2 A-band nightglow VER. Within 86–98 km, the retrieved VER ranges from 717.16 to 2984.27 photons cm^{-3} s^{-1}. The relative posterior 1σ uncertainty ranges from 0.94% to 10.75%, with a mean relative uncertainty of 4.38%. The maximum relative uncertainty occurs at 86 km, where the retrieved VER is relatively low.

The corresponding SABER event is 127076, observed at 03:22:16 UTC on 10 May 2025 at 54.46°N and 117.71°W. Within 86–98 km, the HDI-retrieved temperature ranges from 154.34 to 192.62 K, while the SABER temperature ranges from 153.06 to 188.40 K. Both profiles show a cold structure near 90–94 km and a temperature increase over 96–98 km, indicating that the HDI retrieval can capture the main vertical temperature variations in the local NH MLT. The HDI–SABER temperature differences range from −3.60 to 8.42 K, with a mean absolute difference of 4.56 K. The posterior 1σ uncertainty of the HDI temperature ranges from 1.31 to 4.11 K, with a mean value of 2.32 K; the largest uncertainty occurs at 86 km.

The DOFS results show that the VER DOFS is also close to 1.000 at all altitude levels from 86 to 98 km in this case. Although the observed signal is weaker and the retrieved VER is lower at 86 km, the temperature DOFS at this altitude still reaches 0.910, indicating that the fine spectral structure of the HDI O_2 A-band measurements provides useful information for temperature retrieval even under weak lower-altitude signal conditions. The representative SH and NH cases both demonstrate that fine O_2 A-band nightglow spectral structures measured by HDI can simultaneously constrain VER and temperature under weak nightglow conditions.

https://doi.org/10.5194/egusphere-2026-5511
Preprint. Discussion started: 16 September 2026

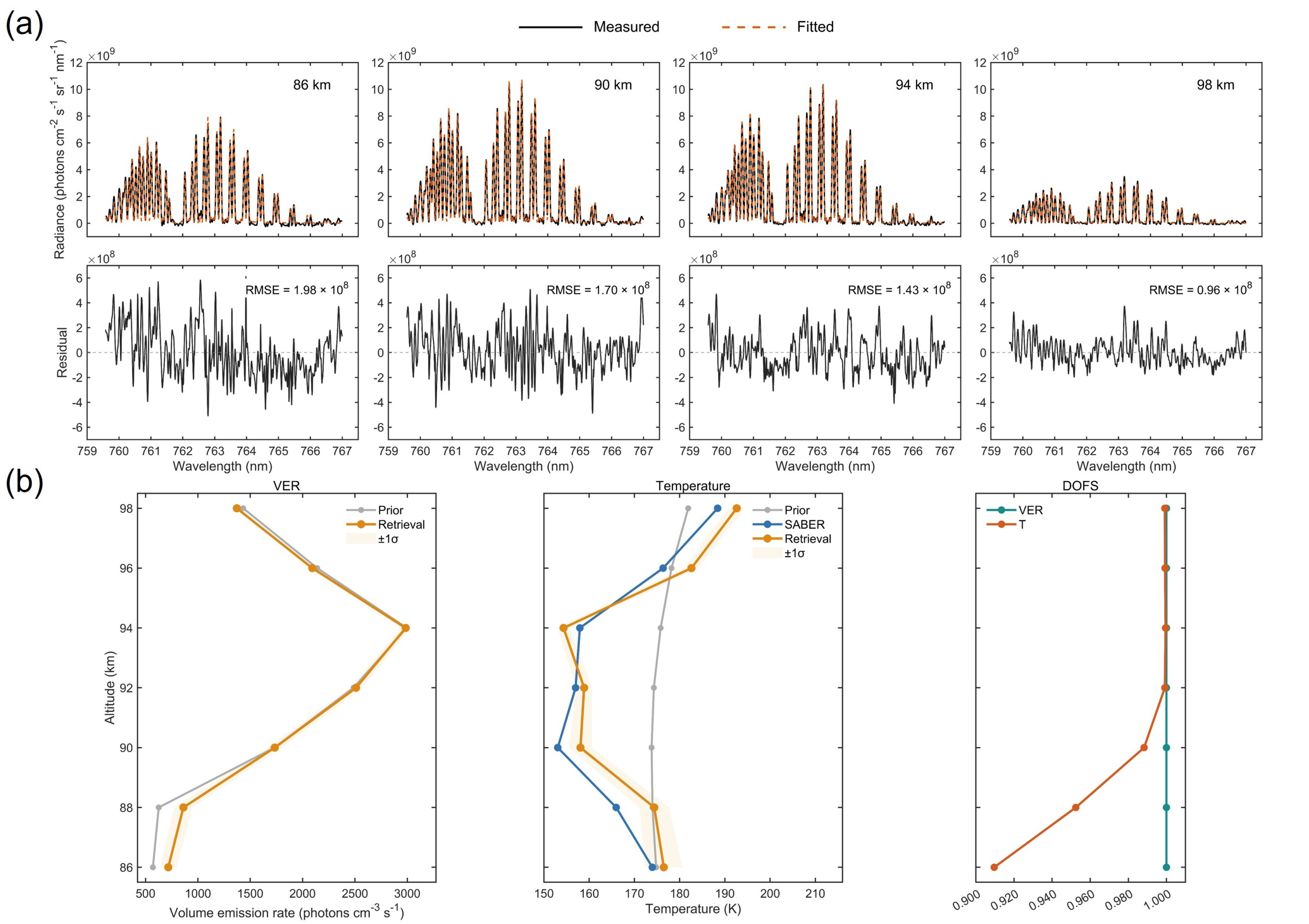

Figure 4. Same as Figure 3, but for a NH HDI observation. The HDI observation was acquired at 05:21:58 UTC on 10 May 2025 at 55.07°N, 116.38°W. The collocated SABER event is 127076, observed at 03:22:16 UTC on 10 May 2025 at 54.46°N, 117.71°W.

3.2 Window-averaged latitude–altitude distributions of HDI O_2 A-band nightglow VER

Building on the representative single-frame retrievals, we further analysed the latitude–altitude averaged distributions of HDI O_2 A-band nightglow VER during the four observation windows from May to August 2025. Figure 5 shows the window-averaged VER distributions over 86–98 km, with a vertical spacing of approximately 2 km. Valid retrieved profiles within each window were averaged onto 1° latitude bins. The observation windows of 8–14 May, 19–25 June, 12–18 July, and 1–7 August include 6128, 6770, 7475, and 8532 valid VER profiles, respectively. Although long Earth-shadow dormancy periods occurred during HDI nighttime observations, the approximately 11 s interval between adjacent frames still provided several thousand valid profiles in each observation window.

https://doi.org/10.5194/egusphere-2026-5511
Preprint. Discussion started: 16 September 2026

Figure 5a shows the SH results. The valid latitude coverages for the four windows are 83°S–49°S, 83°S–55°S, 83°S–34°S, and 83°S–31°S, respectively. The strongest SH VER enhancement occurs during 8–14 May, with elevated emissions extending over approximately 50–80°S and mainly confined to 88–94 km. The peak appears near 62°S and 90 km, with a maximum VER of 3881.03 photons cm^{-3} s^{-1}. During this window, VER increases from 86 to 90 km, forms a relatively broad main emitting layer near 90–92 km, and then decreases above 94 km. In contrast, the SH mid- to high-latitude VER is substantially weaker during June–August. The enhanced regions no longer exhibit the broad, continuous latitudinal structure observed in May, but instead appear mainly as localized narrow bands or enhancements near the latitude boundaries. In June, a localized upper-level enhancement appears near 60°S, but the maximum VER near 90 km over 83°S–60°S is only 1679.09 photons cm^{-3} s^{-1}. In July, the main enhancement is concentrated at 50–60°S and 86–90 km, while the upper-level signal is generally weak. In August, apart from a localized enhancement near 98 km close to the low-latitude boundary, the mid- to high-latitude region is still dominated by relatively weak enhancement near 90 km, with a representative maximum of 2285.59 photons cm^{-3} s^{-1}.

Figure 5b shows the NH results. The valid latitude coverages for the four windows are 47°N–57°N, 43°N–51°N, 26°N–54°N, and 28°N–57°N, respectively. In contrast to the SH enhancement centered near 90 km in May, the strong NH emissions generally occur at higher altitudes. In May, the NH enhancement is mainly located at 92–96 km. In June, VER increases with altitude, with the high-value region concentrated at 96–98 km. In July, the upper-level NH enhancement is most pronounced, forming a distinct strong-emission region over approximately 40–55°N and 96–98 km. The maximum value in Figure 5 occurs near 52°N and 98 km, reaching 4921.13 photons cm^{-3} s^{-1}. In August, the upper-level enhancement remains evident, although the peak intensity is lower than in July. The enhanced region becomes broader in latitude and is mainly distributed over 30–55°N and 94–98 km.

Overall, Figure 5 demonstrates that the HDI-retrieved O_2 A-band nightglow VER exhibits clear latitude–altitude layered structures, with substantial differences among observation windows and between the SH and NH. The main enhancement altitudes in the four windows are distributed over approximately 88–98 km, with local peak VER values of about 2162.15 to 4921.13 photons cm^{-3} s^{-1}. Because O_2 A-band nightglow is primarily controlled by recombination chemistry involving atomic oxygen through the Barth mechanism in the MLT, the retrieved VER altitude distributions and intensity levels are consistent with the emitting-layer altitudes and VER ranges reported by previous O_2 A-band nightglow models (Sheese, 2011; Kaufmann et al., 2018; Deiml, 2017). Meanwhile, the differences in vertical structure between the SH and NH and among different observation windows are also physically consistent with the latitude–altitude distributions and seasonal altitude variations of the MLT atomic oxygen layer revealed by previous atomic oxygen observations (Zhu and Kaufmann, 2019).

https://doi.org/10.5194/egusphere-2026-5511
Preprint. Discussion started: 16 September 2026

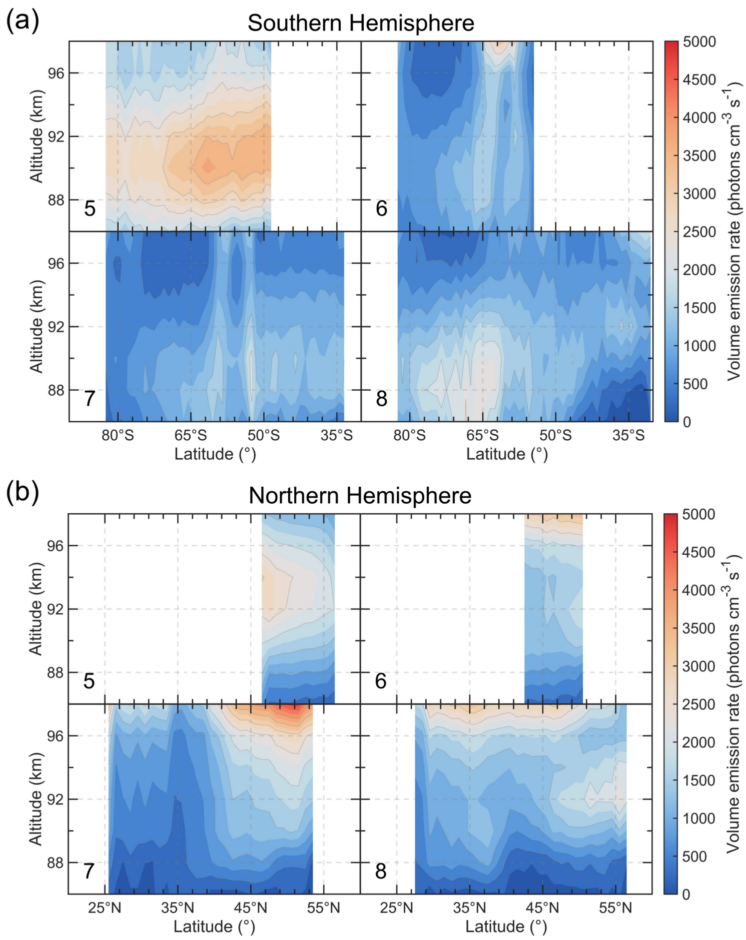

Figure 5. Window-averaged latitude–altitude distributions of HDI O_2 A-band nightglow VER. (a) SH results. **(b)** NH results. In each panel, the upper-left, upper-right, lower-left, and lower-right subplots correspond to the four observation windows of 8–14 May, 19–25 June, 12–18 July, and 1–7 August 2025, respectively. The four windows include 6128, 6770, 7475, and 8532 valid VER profiles, respectively, averaged onto 1° latitude bins over 86–98 km with a vertical spacing of 2 km. The valid SH latitude ranges are 83°S–49°S, 83°S–55°S, 83°S–34°S, and 83°S–31°S, respectively, while the valid NH latitude ranges are 47°N–57°N, 43°N–51°N, 26°N–54°N, and 28°N–57°N. Blank areas indicate latitude–altitude grids without valid retrievals.

3.3 Comparison of HDI and SABER latitude–altitude temperature distributions

We further compared the HDI-retrieved temperatures with SABER temperature products within the same observation windows. For each window, the original SABER temperature profiles were first interpolated vertically onto the HDI retrieval altitude grid, spanning 86–98 km with a spacing of 2 km. The interpolated SABER temperature profiles were then window-averaged onto the same 1° latitude bins used for HDI, yielding SABER temperature fields on the same latitude–altitude grids as the HDI retrievals. The HDI temperature profiles were averaged using the same 1° latitude grid. Figure 6 shows the latitude–altitude

https://doi.org/10.5194/egusphere-2026-5511
Preprint. Discussion started: 16 September 2026

distributions of HDI temperature, SABER temperature, and their differences during the four observation windows from May to August 2025. The HDI temperature fields represent averages over all valid HDI profiles in each window, with the number of averaged profiles identical to that used for the VER fields. In contrast, the SABER temperature fields and the difference fields are shown only for latitude–altitude grids where both HDI and SABER data are valid; all difference statistics are also calculated only over these common valid grids.

After applying the common-valid-coverage criterion, the numbers of HDI profiles used for the temperature comparison in May, June, July, and August are 1858, 6770, 7475, and 8229, respectively, while the corresponding numbers of SABER profiles are 1714, 2579, 5718, and 6071. The limitation of SABER coverage is most evident in the SH in May, when the common valid latitude range is restricted to 54°S–49°S. In August, part of the high-latitude side of the NH HDI observation region is also not covered by collocated SABER measurements, resulting in a common valid latitude range of 28°N–54°N, slightly narrower than the original valid HDI observation range (Remsberg et al., 2008). Apart from these cases, the common valid latitude ranges in the other windows are generally consistent with the main valid HDI observation ranges for the corresponding windows.

The SH results are shown in Figures 6a, 6c, and 6e. Overall, both HDI and SABER show a vertical structure characterized by relatively warm temperatures at 86–90 km and colder temperatures at 94–98 km, with temperature generally decreasing with altitude. Within the common valid grids, the maximum HDI temperatures in the four SH windows range from 206.61 to 215.80 K, while the maximum SABER temperatures range from 202.89 to 211.34 K; in both datasets, the maxima occur near 86 km. The corresponding temperature difference distributions indicate that the SABER–HDI differences remain within a relatively small range overall, with localized alternating positive and negative patterns. The mean absolute differences from May to August are 2.43, 3.12, 3.62, and 3.57 K, respectively, and the corresponding maximum absolute differences are 5.75, 6.12, 5.61, and 5.73 K.

The NH results are shown in Figures 6b, 6d, and 6f. In contrast to the SH, both the HDI and SABER temperature fields in the NH exhibit relatively higher temperatures at upper altitudes, with the maximum temperatures mainly occurring near 98 km. Within the common valid grids, the maximum HDI temperatures in the four NH windows range from 190.47 to 205.25 K, while the maximum SABER temperatures range from 190.40 to 206.08 K. The corresponding difference distributions also show localized alternating positive and negative patterns, while the overall amplitudes remain limited. The mean absolute differences from May to August are 2.14, 3.48, 3.82, and 3.19 K, respectively, and the corresponding maximum absolute differences are 5.54, 6.02, 5.57, and 5.63 K.

The difference fields show localized alternating positive and negative differences across latitude and altitude. Because the common valid coverage is larger for the SH during June–August and for the NH during July–August, more pronounced local structures are visible in these difference fields. Nevertheless, the maximum absolute differences are only 5.54–6.12 K, indicating that these local differences do not lead to a substantial systematic offset. It should also be noted that the approximately 11 s interval between adjacent HDI frames provides dense temperature sampling over nearby geographic regions, and part of the local small-scale structure may remain after window averaging. In contrast, the SABER temperature

https://doi.org/10.5194/egusphere-2026-5511
Preprint. Discussion started: 16 September 2026

products and the corresponding window-averaged fields are generally smoother. Differences in viewing geometry, sampling time, vertical response, and spatial averaging between the two instruments may also contribute to localized variations in the difference fields.

Overall, the SH and NH results show that HDI and SABER capture consistent dominant temperature stratification and latitude–altitude variations over 86–98 km. In the SH, both datasets show relatively warmer temperatures at lower altitudes and colder temperatures at upper altitudes, whereas in the NH both datasets exhibit a relative temperature enhancement near 98 km. The SABER – HDI differences are mainly characterized by localized alternating positive and negative patterns, rather than by an overall systematic bias.

https://doi.org/10.5194/egusphere-2026-5511
Preprint. Discussion started: 16 September 2026

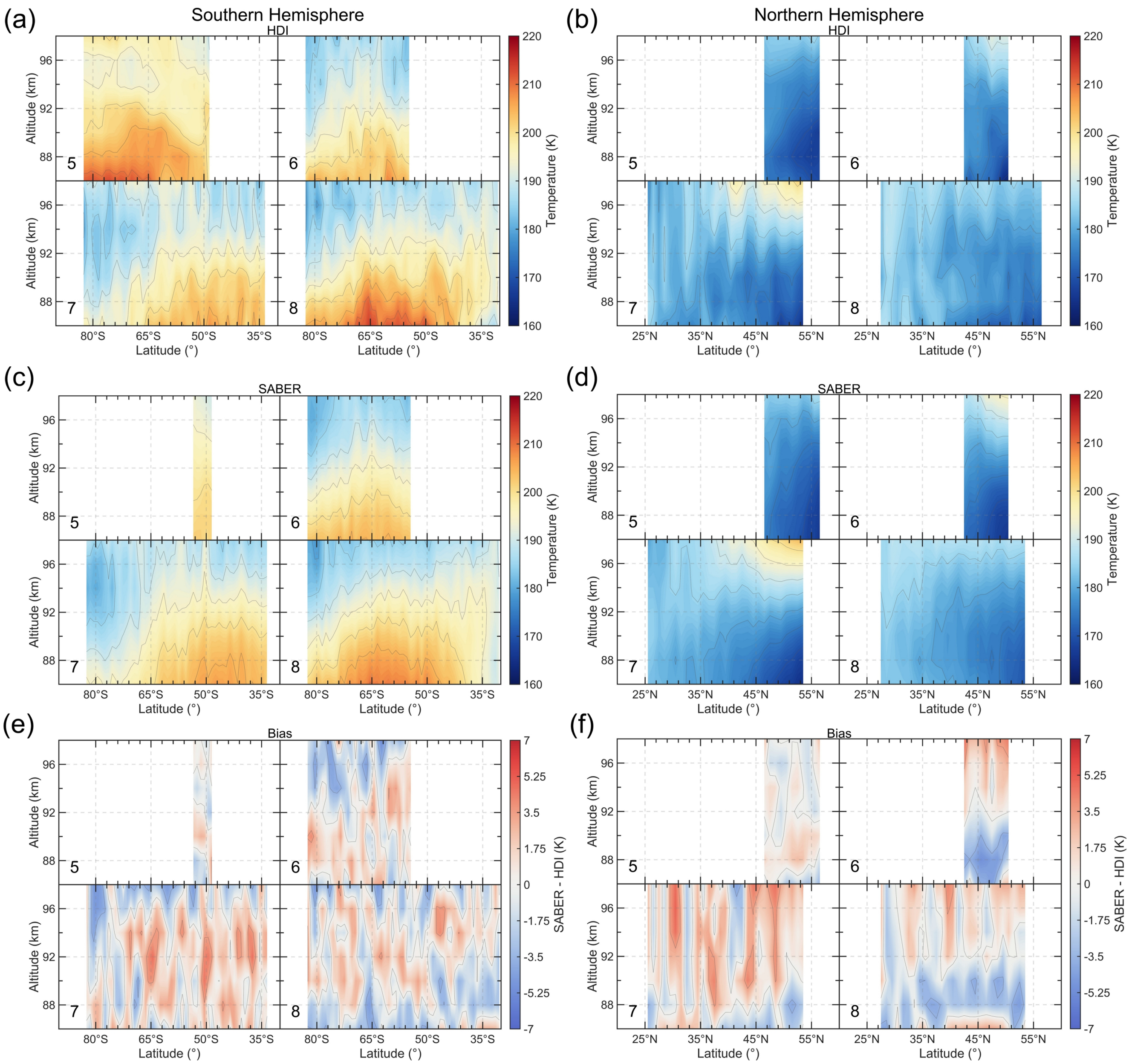

Figure 6. Comparison of HDI and SABER latitude–altitude temperature distributions. (a), (b) HDI-retrieved temperatures in the SH and NH, respectively. **(c), (d)** SABER temperatures within the same observation windows in the SH and NH, respectively. **(e), (f)** Temperature differences in the SH and NH, respectively, defined as SABER − HDI. The ordering of the four observation windows, the latitude–altitude grids, and the valid retrieval ranges in each panel are the same as in Figure 5. The HDI temperature panels show window-averaged results from all valid HDI profiles. The SABER temperature and difference panels are shown only for grids where both HDI and SABER data are valid. The numbers of HDI profiles used for the May–August temperature comparisons are 1858, 6770, 7475, and 8229, respectively, and the corresponding numbers of SABER profiles are 1714, 2579, 5718, and 6071.

https://doi.org/10.5194/egusphere-2026-5511
Preprint. Discussion started: 16 September 2026

3.4 Posterior uncertainty and DOFS assessment of HDI O_2 A-band nightglow retrievals

To further assess the reliability of the HDI O_2 A-band nightglow VER retrievals, we analysed the posterior 1σ uncertainty of VER and its percentage relative to the retrieved VER. Because the VER DOFS is generally close to 1 within the main valid emitting layer, indicating strong observational constraints on the VER retrieval, this section evaluates the retrieval stability mainly in terms of absolute posterior uncertainty and relative uncertainty.

The posterior 1σ uncertainty of the HDI-retrieved VER remains low overall, mainly within approximately 20–80 photons cm^{-3} s^{-1}, and shows a clear altitude dependence. The mean 1σ uncertainties in the SH from May to August are 43.87, 30.80, 29.94, and 32.26 photons cm^{-3} s^{-1}, respectively, with corresponding mean relative 1σ uncertainties of 1.90%, 3.45%, 3.59%, and 4.04%. In the NH, the mean 1σ uncertainties from May to August are 40.30, 42.58, 42.40, and 40.83 photons cm^{-3} s^{-1}, respectively, with corresponding mean relative 1σ uncertainties of 3.83%, 4.33%, 7.06%, and 6.99%. The largest uncertainties mainly occur near 86–88 km. Combining the SH and NH statistics, the mean relative 1σ uncertainties from May to August are 2.36%, 3.66%, 4.86%, and 5.09%, respectively. The maximum relative uncertainty does not exceed 45% and occurs mainly near the lower-altitude boundary or in localized weak-VER regions (Fig. 7). In contrast, the relative uncertainties are generally lower within the main nightglow emitting layer and in regions with stronger VER. The enhanced relative uncertainties at lower altitudes and in weak-signal regions mainly reflect the amplification of the uncertainty-to-signal ratio, rather than an anomalous increase in the absolute posterior uncertainty. These results demonstrate that fine HDI O_2 A-band spectral measurements provide stable and effective observational constraints for nighttime VER retrievals in the MLT.

https://doi.org/10.5194/egusphere-2026-5511
Preprint. Discussion started: 16 September 2026

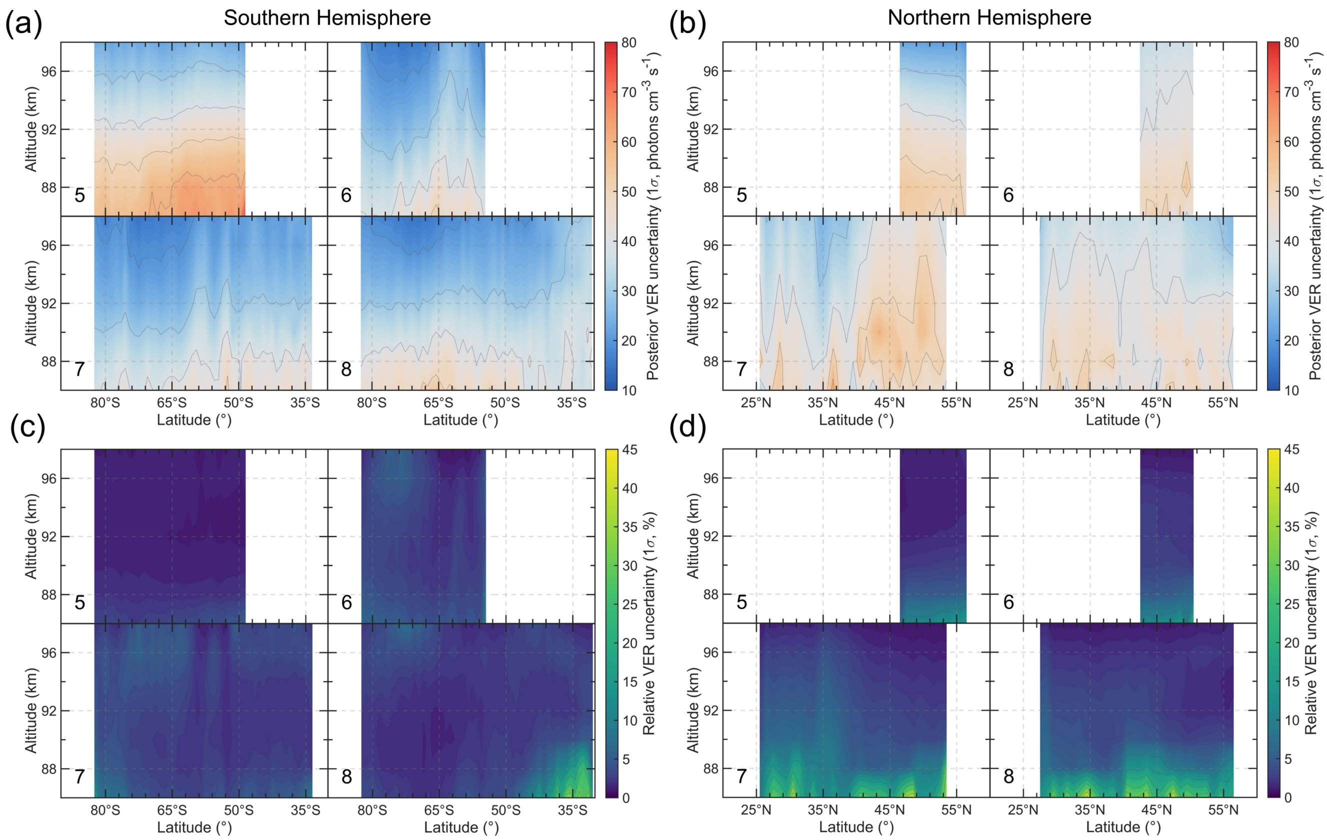

Figure 7. Posterior uncertainties of HDI O_2 A-band nightglow VER retrievals. (a), (b) Latitude–altitude distributions of the VER posterior 1σ uncertainty in the SH and NH, respectively. **(c), (d)** Latitude–altitude distributions of the relative VER posterior 1σ uncertainty in the SH and NH, respectively, defined as 100 × σ_{VER} / VER (%). The ordering of the four nighttime observation windows, the latitude–altitude grids, and the valid retrieval ranges in each panel are the same as in Figure 5.

To assess the reliability of the HDI O_2 A-band nightglow temperature retrievals, we analysed the posterior 1σ uncertainty and DOFS of the retrieved temperatures. Figure 8 shows the latitude–altitude distributions of the posterior 1σ temperature uncertainty (Figs. 8a–b) and the corresponding temperature DOFS (Figs. 8c–d) for the four nighttime observation windows from May to August 2025.

The posterior 1σ uncertainty of the HDI temperature retrievals remains low overall, mainly within 2–5 K, and is below 7 K for all valid grids. The mean posterior 1σ temperature uncertainties in the SH from May to August are 2.42, 3.62, 3.46, and 3.65 K, respectively. In the NH, the corresponding values are 2.65, 2.85, 3.34, and 3.26 K. Combining the SH and NH statistics, the mean posterior temperature uncertainties from May to August are 2.47, 3.44, 3.41, and 3.51 K, respectively. Overall, the HDI temperature retrievals maintain stable posterior uncertainty levels across the four nighttime observation windows.

The temperature DOFS remains high over most valid regions, with localized reductions mainly occurring near the lower-altitude boundary or in weak-emission regions. Combining the SH and NH statistics, the mean temperature DOFS values from

https://doi.org/10.5194/egusphere-2026-5511
Preprint. Discussion started: 16 September 2026

May to August are 0.980, 0.948, 0.952, and 0.946, respectively, with corresponding minimum values of 0.849, 0.850, 0.852, and 0.850. The mean DOFS over all months and both hemispheres is 0.954, and 89.31% of the valid grids have DOFS values not lower than 0.90.

Spatially, regions with lower posterior temperature uncertainties in Figs. 8a–b generally correspond to regions with higher temperature DOFS in Figs. 8c–d, and are spatially consistent with the VER enhancement regions shown in Figure 5. The main nightglow emitting layer and regions with stronger VER usually provide clearer rotational spectral structures, resulting in lower temperature uncertainties and higher DOFS. In contrast, weak-emission layers and altitude-boundary regions exhibit higher uncertainties and lower DOFS. Taken together, these results indicate that fine HDI O_2 A-band spectral measurements provide effective information-content constraints for MLT temperature retrievals.

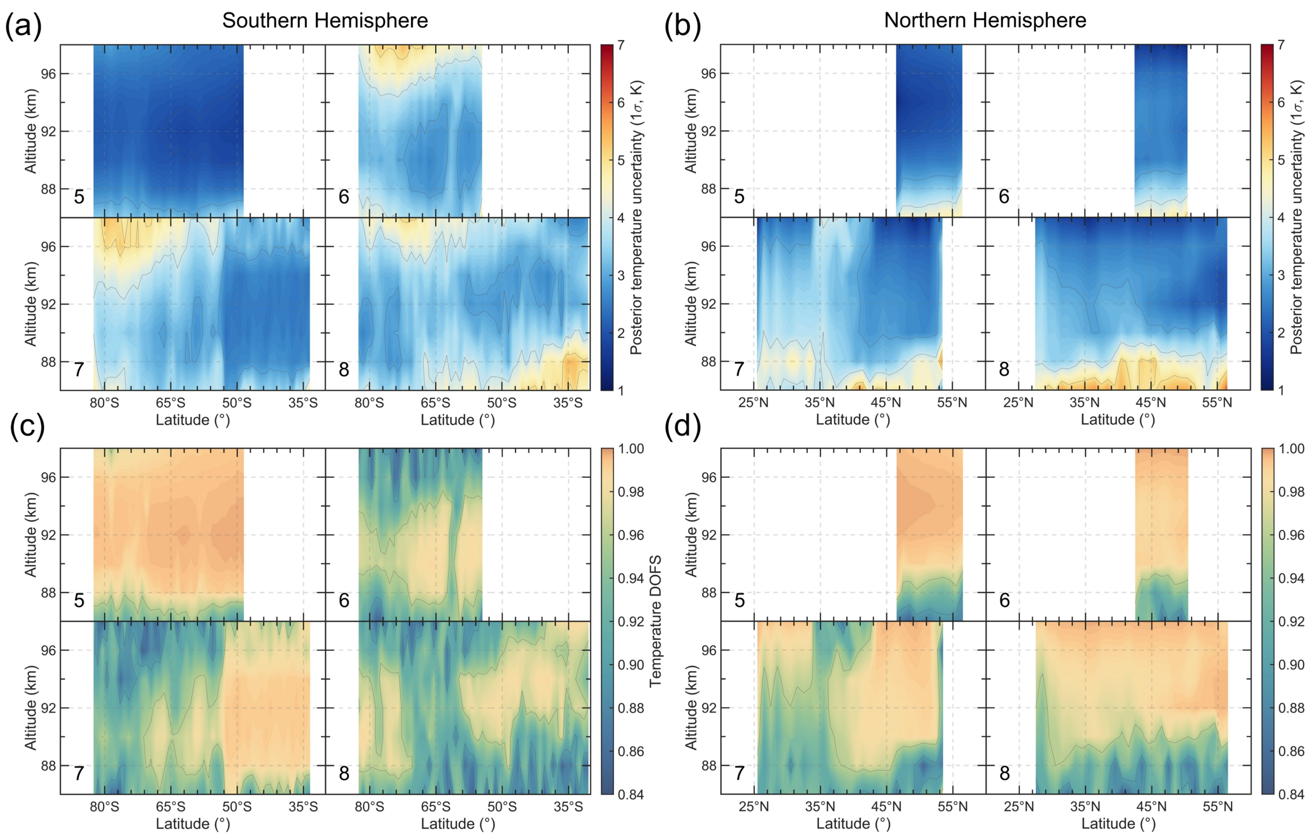

Figure 8. Posterior uncertainty and information content of HDI O_2 A-band nightglow temperature retrievals. (a), (b) Latitude–altitude distributions of the posterior 1σ temperature uncertainty in the SH and NH, respectively. **(c), (d)** Latitude–altitude distributions of temperature DOFS in the SH and NH, respectively. The ordering of the four nighttime observation windows, the latitude–altitude grids, and the valid retrieval ranges in each panel are the same as in Figure 5.

https://doi.org/10.5194/egusphere-2026-5511
Preprint. Discussion started: 16 September 2026

Discussion and conclusion

The present analysis reflects the early operational phase of the HDI mission rather than the full observational capability of the instrument. Nighttime observations are currently constrained by the observing strategy during Earth-shadow segments, non-imaging intervals, orbital sampling, solar-zenith-angle screening, and the availability of sufficiently strong nightglow emissions. Consequently, the May–August dataset represents regional observations obtained within limited nighttime sampling windows instead of continuous monthly means or global climatological coverage. The primary objective of this study is therefore to establish the feasibility and observational capability of hyperspectral O_2 A-band measurements for simultaneous retrieval of VER and temperature in the nighttime MLT, providing the first on-orbit demonstration of the proposed retrieval framework rather than a comprehensive characterization of global MLT variability.

In the current stage of the HDI mission, the available observations provide an early effective demonstration of the capability of spaceborne hyperspectral O_2 A-band nightglow measurements for simultaneous retrieval of VER and temperature in the MLT. Although the observational coverage remains limited, the retrieval exhibits consistently stable performance, as reflected by the low spectral fitting residuals, close agreement with SABER temperatures, and high temperature information content. The typical spectral fitting residuals are approximately 1%–3% relative to the observed spectral peak; the window-averaged mean absolute differences between HDI and SABER temperatures are less than 3.82 K; the monthly mean relative posterior 1σ uncertainty of VER is less than 5.09%; the monthly mean posterior 1σ uncertainty of temperature is less than 3.51 K; and the monthly mean temperature DOFS exceeds 0.946, with 89.31% of valid grids having DOFS values not lower than 0.90. These results demonstrate that the fine rotational structures resolved by HDI provide sufficient independent information to simultaneously constrain VER and temperature, highlighting the potential of SHS for quantitative nighttime limb sounding. By deriving VER and temperature from individual hyperspectral measurement, HDI provides intrinsically co-registered and internally consistent constraints for subsequent atomic oxygen retrievals, reducing potential inconsistencies associated with the use of separately observed temperature profiles.

The present analysis also provides insight into the factors controlling retrieval performance. Larger posterior temperature uncertainties and reduced DOFS occur mainly near the lower retrieval boundary and in regions with weak nightglow emissions, indicating that retrieval quality is strongly governed by the available spectral information and measurement signal-to-noise ratio. Consequently, the effective retrieval range is ultimately determined by the combined influence of airglow intensity, spectral sensitivity to temperature, and observational conditions. Future optimization of the observing strategy during Earth-shadow segments, together with reduced non-imaging periods and expanded nighttime sampling, is expected to improve the spatial representativeness and temporal continuity of the observations, particularly at middle and low latitudes. These improvements will further enhance the capability of HDI for long-term monitoring of nighttime MLT thermal structure and airglow variability.

In this study, the main analysis is restricted to 86–98 km, considering the nightglow signal intensity, consistency of valid altitude coverage, and retrieval stability. Further work is needed to systematically evaluate the spectral signal quality, retrieval

https://doi.org/10.5194/egusphere-2026-5511
Preprint. Discussion started: 16 September 2026

uncertainty, and quality-screening criteria for altitude levels above 98 km, in order to assess their retrievability under different observing conditions. Extending the retrieval to these altitude levels would improve the capability of HDI to characterize the upper structure of the O_2 A-band emission layer and provide additional observational constraints for studies of nighttime temperature variability and oxygen-related photochemical processes in the MLT.

Beyond the current demonstration, HDI provides relatively stable nighttime coverage at high SH latitudes and may serve as a complementary observation source during periods when SABER overpass timing or spatial sampling is limited. With the accumulation of future observations, HDI data are expected to support more comprehensive joint analyses of O_2 A-band nightglow VER, MLT temperature fields, and atomic-oxygen-related processes. Combined with SABER, empirical models, and photochemical models, these data can enable more systematic cross-validation and provide new observational constraints for studies of nighttime thermal structure, nightglow variability, and dynamical–chemical coupling processes of the MLT.

Data availability

The SABER temperature datasets are available from https://saber.gats-inc.com/browse_data.php#. The HDI Level-1 data and the retrieved temperature and VER datasets of this study are not publicly available due to institutional ownership and data policy restrictions, but are available from the corresponding author upon reasonable request.

Author contributions

GZ designed the forward model and retrieval algorithm, performed the data analysis, and drafted the manuscript. HL, WX, and ZL conceived the study and were responsible for project administration. Q Wang and YQ processed the HDI Level-1 data products. HL, WX, ZL, Q Wu, and YD contributed to the design and development of the HDI instrument. HL, WX, and WL contributed to the revision of the manuscript. GZ finalized the manuscript with contributions and feedback from all co-authors.

Competing interests

The authors declare that they have no conflict of interest.

Disclaimer

https://doi.org/10.5194/egusphere-2026-5511
Preprint. Discussion started: 16 September 2026

Acknowledgements

We sincerely thank Dr. Cheng Chen from the Anhui Institute of Optics and Fine Mechanics, Hefei Institutes of Physical Science, Chinese Academy of Sciences, for his careful review of the manuscript and his valuable comments and constructive suggestions.

Financial support

This research is supported by the National Natural Science Foundation of China (Grant number 42475140) and the National Key Research and Development Program of China (Grant numbers 2022YFB3901800, 2022YFB3901803).

References

Chen, Q., Ntokas, K., Linder, B., Krasauskas, L., Ern, M., Preusse, P., Ungermann, J., Becker, E., Kaufmann, M., and Riese, M.: Satellite observations of gravity wave momentum flux in the mesosphere and lower thermosphere (MLT): feasibility and requirements, Atmospheric Measurement Techniques, 15, 7071–7103, 2022.

Deiml, M.: Development of a small satellite remote sensing payload for passive limb sounding of the atmospheric oxygen emission, Bergische Universität Wuppertal, 2017.

Gumbel, J., Megner, L., Christensen, O. M., Ivchenko, N., Murtagh, D. P., Chang, S., Dillner, J., Ekebrand, T., Giono, G., and Hammar, A.: The MATS satellite mission–gravity wave studies by Mesospheric Airglow/Aerosol Tomography and Spectroscopy, Atmospheric Chemistry and Physics, 20, 431–455, 2020.

Hamidouche, M. and Lichtenberg, G.: In-flight retrieval of SCIAMACHY instrument spectral response function, Remote Sensing, 10, 401, 2018.

Hays, P. B., Kafkalidis, J. F., Skinner, W. R., and Roble, R. G.: A global view of the molecular oxygen night airglow, Journal of Geophysical Research: Atmospheres, 108, 2003.

He, M. and Forbes, J. M.: Rossby wave second harmonic generation observed in the middle atmosphere, Nature Communications, 13, 7544, 2022.

Jia, J., Murberg, L. E., Løvset, T., Orsolini, Y. J., Espy, P. J., Zeller, L. C., Salinas, C. C. J. H., Lee, J. N., Wu, D., and Zhang, J.: Energetic particle precipitation influences global secondary ozone distribution, Communications Earth & Environment, 5, 270, 2024.

https://doi.org/10.5194/egusphere-2026-5511
Preprint. Discussion started: 16 September 2026

Kalogerakis, K. S.: A previously unrecognized source of the O2 Atmospheric band emission in Earth's nightglow, Science Advances, 5, eaau9255, 2019.

Katsuda, S., Enoto, T., Lommen, A. N., Mori, K., Motizuki, Y., Nakajima, M., Ruhl, N. C., Sato, K., Stober, G., and Tashiro, M. S.: Long-term density trend in the mesosphere and lower thermosphere from occultations of the Crab Nebula with X-ray astronomy satellites, Journal of Geophysical Research: Space Physics, 128, e2022JA030797, 2023.

Kaufmann, M., Olschewski, F., Mantel, K., Solheim, B., Shepherd, G., Deiml, M., Liu, J., Song, R., Chen, Q., and Wroblowski, O.: A highly miniaturized satellite payload based on a spatial heterodyne spectrometer for atmospheric temperature measurements in the mesosphere and lower thermosphere, Atmospheric Measurement Techniques, 11, 3861–3870, 2018.

Kochanov, R. V., Gordon, I., Rothman, L., Wcisło, P., Hill, C., and Wilzewski, J.: HITRAN Application Programming Interface (HAPI): A comprehensive approach to working with spectroscopic data, Journal of Quantitative Spectroscopy and Radiative Transfer, 177, 15–30, 2016.

Kvifte, G.: Atmospheric Oxygen Bands in Emission from Neon–Oxygen Mixtures, and in Night Sky and Auroral Luminescences, Nature, 168, 741–742, 1951.

Li, H., Feng, Y., Li, F., Wang, H., Hu, X., He, W., and Wu, K.: A new Einstein coefficient method for mesopause–lower thermosphere atmosphere temperature retrieval under a non-local thermal equilibrium situation, Optics Express, 31, 30413–30434, 2023.

Linder, B., Krasauskas, L., Megner, L., and Murtagh, D. P.: The global O2 airglow field as seen by the MATS satellite: strong equatorial maximum and planetary wave influence, Atmospheric Chemistry and Physics, 25, 12843–12851, 2025.

Liou, K.-N.: An introduction to atmospheric radiation, Academic press2002.

Liu, J.: Study on a miniaturized satellite payload for atmospheric temperature measurements, Dissertation, Wuppertal, Bergische Universität, 2019, 2019.

Luo, H., Xiong, W., Li, Z., and Shi, H.: Optical Design and Performance Verification of Space-Borne Near-Space Hyperspectral Atmospheric Density Profile Imager (Invited), Acta Optica Sinica, 45, 1801013–1801013–1801012, 2025.

Noll, S., Kausch, W., Kimeswenger, S., Unterguggenberger, S., and Jones, A. M.: Comparison of VLT/X-shooter OH and O 2 rotational temperatures with consideration of TIMED/SABER emission and temperature profiles, Atmospheric Chemistry and Physics, 16, 5021–5042, 2016.

Ntokas, K., Ungermann, J., Kaufmann, M., Neubert, T., and Riese, M.: Observation of horizontal temperature variations by a spatial heterodyne interferometer using single-sided interferograms, Atmospheric measurement techniques, 16, 5681–5696, 2023.

Picone, J., Hedin, A., Drob, D. P., and Aikin, A.: NRLMSISE-00 empirical model of the atmosphere: Statistical comparisons and scientific issues, Journal of Geophysical Research: Space Physics, 107, SIA 15–11–SIA 15–16, 2002.

Plane, J. M., Feng, W., and Dawkins, E. C.: The mesosphere and metals: Chemistry and changes, Chemical reviews, 115, 4497–4541, 2015.

https://doi.org/10.5194/egusphere-2026-5511
Preprint. Discussion started: 16 September 2026

Remsberg, E. E., Marshall, B., Garcia-Comas, M., Krueger, D., Lingenfelser, G., Martin-Torres, J., Mlynczak, M., Russell III, J., Smith, A., and Zhao, Y.: Assessment of the quality of the Version 1.07 temperature-versus-pressure profiles of the middle atmosphere from TIMED/SABER, Journal of Geophysical Research: Atmospheres, 113, 2008.

Richter, H., Buchbender, C., Güsten, R., Higgins, R., Klein, B., Stutzki, J., Wiesemeyer, H., and Hübers, H.-W.: Direct measurements of atomic oxygen in the mesosphere and lower thermosphere using terahertz heterodyne spectroscopy, Communications Earth & Environment, 2, 19, 2021.

Rodgers, C. D.: Inverse methods for atmospheric sounding: theory and practice, World scientific2000.

Russell, J. P. and Lowe, R.: Atomic oxygen profiles (80–94 km) derived from Wind Imaging Interferometer/Upper Atmospheric Research Satellite measurements of the hydroxyl airglow: 1. Validation of technique, Journal of Geophysical Research: Atmospheres, 108, 2003.

Sheese, P.: Mesospheric ozone densities retrieved from OSIRIS observations of the O_2A-band dayglow, Library and Archives Canada= Bibliothèque et Archives Canada, Ottawa2011.

Sheese, P., Llewellyn, E., Gattinger, R., Bourassa, A., Degenstein, D., Lloyd, N., and McDade, I.: Temperatures in the upper mesosphere and lower thermosphere from OSIRIS observations of O2 A-band emission spectra, Canadian Journal of Physics, 88, 919–925, 2010.

Shi, H., Li, Z., Ye, H., Luo, H., Xiong, W., and Wang, X.: First level 1 product results of the greenhouse gas monitoring instrument on the GaoFen-5 satellite, IEEE Transactions on Geoscience and Remote Sensing, 59, 899–914, 2020.

Stevens, M., Englert, C., Harlander, J., Marr, K., Harding, B., Triplett, C., Mlynczak, M., Yuan, T., Evans, J., and Mende, S.: Temperatures in the upper mesosphere and lower thermosphere from O2 atmospheric band emission observed by ICON/MIGHTI, Space Science Reviews, 218, 67, 2022.

Sun, K., Gordon, I. E., Sioris, C. E., Liu, X., Chance, K., and Wofsy, S. C.: Reevaluating the Use of O2 a 1Δ g Band in Spaceborne Remote Sensing of Greenhouse Gases, Geophysical Research Letters, 45, 5779–5787, 2018.

Sun, K., Yousefi, M., Chan Miller, C., Chance, K., González Abad, G., Gordon, I. E., Liu, X., O'Sullivan, E., Sioris, C. E., and Wofsy, S. C.: An optimal estimation-based retrieval of upper atmospheric oxygen airglow and temperature from SCIAMACHY limb observations, Atmospheric Measurement Techniques Discussions, 2022, 1–37, 2022.

van Caspel, W. E., Espy, P., Hibbins, R., Stober, G., Brown, P., Jacobi, C., and Kero, J.: A case study of the solar and lunar semidiurnal tide response to the 2013 sudden stratospheric warming, Journal of Geophysical Research: Space Physics, 128, e2023JA031680, 2023.

Wu, K., Li, H., Su, J., Wang, D., Wang, Z., and He, W.: Retrieval of Temperature Profiles in the MLT Region Using the O 2 (b 1 Σ) Airglow With Spectral Contamination Correction of N 2 1 PG Emissions, IEEE Transactions on Geoscience and Remote Sensing, 62, 1–13, 2024.

Wu, X., Zhu, Y., Smith, A. K., Kaufmann, M., Jiang, G., Liu, S., and Xu, J.: A new data set of nighttime chemical heating rates in the upper mesosphere and lower thermosphere derived from SCIAMACHY OH (9–6) emissions and SABER profiles, Atmospheric Chemistry and Physics, 26, 4669–4683, 2026.

https://doi.org/10.5194/egusphere-2026-5511
Preprint. Discussion started: 16 September 2026

Xing, C., Wei, S., Li, Y., Jiao, P., Liu, C., Chen, J., Wang, W., Peng, H., Song, Y., and Liu, C.: Fast-hyperspectral imaging remote sensing: Emission quantification of NO_2 and SO_2 from marine vessels, Light: Science & Applications, 14, 308, 2025.

Yu, S., Drouin, B. J., and Miller, C. E.: High resolution spectral analysis of oxygen. IV. Energy levels, partition sums, band constants, RKR potentials, Franck-Condon factors involving the X3Σg−, a1Δg and b1Σg+ states, The Journal of Chemical Physics, 141, 2014.

Zarboo, A., Bender, S., Burrows, J. P., Orphal, J., and Sinnhuber, M.: Retrieval of O 2 (1∑) and O 2 (1 Δ) volume emission rates in the mesosphere and lower thermosphere using SCIAMACHY MLT limb scans, Atmospheric Measurement Techniques, 11, 2018.

Zhu, Y. and Kaufmann, M.: Consistent nighttime atomic oxygen concentrations from O_2 A-band, O (1S) green-Line, and OH airglow measurements as performed by SCIAMACHY, Geophysical Research Letters, 46, 8536–8545, 2019.